Highly Efficient Solar-Driven Carbon Dioxide Reduction on Molybdenum Disulfide Catalyst Using Choline Chloride-Based Electrolyte

Mohammad Asadi, Mohammad Hossein Motevaselian, Alireza Moradzadeh, Leily Majidi, Mohammadreza Esmaeilirad, Tao Victor Sun, Cong Liu, Rumki Bose, Pedram Abbasi, Peter Zapol, Amid P. Khodadoust, Larry A. Curtiss, Narayana R. Aluru, and Amin Salehi-Khojin**

Conversion of CO_2 to energy-rich chemicals using renewable energy is of much interest to close the anthropogenic carbon cycle. However, the current photoelectrochemical systems are still far from being practically feasible. Here the successful demonstration of a continuous, energy efficient, and scalable solar-driven CO_2 reduction process based on earth-abundant molybdenum disulfide (MoS_2) catalyst, which works in synergy with an inexpensive hybrid electrolyte of choline chloride (a common food additive for livestock) and potassium hydroxide (KOH) is reported. The CO_2 saturated hybrid electrolyte utilized in this study also acts as a buffer solution (pH ≈ 7.6) to adjust pH during the reactions. This study reveals that this system can efficiently convert CO_2 to CO with solar-to-fuel and catalytic conversion efficiencies of 23% and 83%, respectively. Using density functional theory calculations, a new reaction mechanism in which the water molecules near the MoS_2 cathode act as proton donors to facilitate the CO_2 reduction process by MoS_2 catalyst is proposed. This demonstration of a continuous, cost-effective, and energy efficient solar driven CO_2 conversion process is a key step toward the industrialization of this technology.

1. Introduction

For more than 200 years, fossil fuels have sustained our society as an unrivaled source of energy due to their ready availability, stability, and high energy density. However, the increasing CO_2 levels in the atmosphere, along with the ever-increasing energy consumption in modern society, have made the development of renewable energy resources more vital than ever.[1–3] Among the various renewable energy resources, solar energy has unique potential to replace fossil fuels due to its abundance, sustainability, and capability of being harvested.[4–6] However, the main challenge with solar energy is its intermittent and fluctuating nature, which demands a reliable storage method if sunlight is to be utilized as a new large-scale energy source. Among different storage methods, one promising approach is to store the solar energy in the

Prof. M. Asadi, M. Esmaeilirad
Department of Chemical and Biological Engineering
Illinois Institute of Technology
Chicago, IL 60616, USA

M. H. Motevaselian, A. Moradzadeh, T. V. Sun, Prof. N. R. Aluru
Department of Mechanical Science and Engineering
Beckman Institute for Advanced Science and Technology
University of Illinois at Urbana-Champaign
Urbana, IL 61801, USA
E-mail: aluru@illinois.edu

L. Majidi, R. Bose, P. Abbasi, Prof. A. Salehi-Khojin
Department of Mechanical and Industrial Engineering
University of Illinois at Chicago
Chicago, IL 60607, USA
E-mail: salehikh@uic.edu

Dr. C. Liu
Chemical Sciences and Engineering Division
Argonne National Laboratory
Argonne, IL 60439, USA

Dr. P. Zapol, Dr. L. A. Curtiss
Materials Science Division
Argonne National Laboratory
Argonne, IL 60439, USA

Prof. A. P. Khodadoust
Department of Civil and Materials Engineering
University of Illinois at Chicago
Chicago, IL 60607, USA

The ORCID identification number(s) for the author(s) of this article can be found under https://doi.org/10.1002/aenm.201803536.

DOI: 10.1002/aenm.201803536

 © 2019 WILEY-VCH Verlag GmbH & Co. KGaA, Weinheim

form of a burnable feedstock by electrochemical conversion of existing CO_2 in the atmosphere.[5,7–10] This method can provide a versatile way to close the anthropogenic carbon cycle by enabling two-way traffic between CO_2 emissions and solar made chemical fuels.[11–13]

In recent years, there have been numerous efforts to establish a benchmark for solar-to-fuel energy conversion by the photochemical approach.[9–12,14–19] However, the efficiencies for different configurations, including photovoltaic electrolysis (PV/electrolysis) and photoelectrochemical systems do not exceed 13.4%.[11,14,15,18,19] Here, we report the first successful demonstration of an efficient, and scalable flow cell (electrolyzer) that delivers the photocurrent to the catalytic sites in a continuous mode and exhibits solar-to-fuel and catalytic conversion efficiencies of 23% and 83%, respectively. This performance benefits from an inexpensive hybrid electrolyte of choline chloride (a common food additive for livestock and waste product of soybean oil production) and potassium hydroxide (KOH) that works remarkably well with a cathode of molybdenum disulfide nanoflakes (MoS_2 NFs), an earth-abundant transition metal dichalcogenide, and an anode of iridium oxide nanoparticles (IrO_2 NPs).

2. Results and Discussion

The MoS_2 catalyst was synthesized in a chemical vapor transport process followed by a liquid phase exfoliation method.[20–22] The synthesized MoS_2 nanoflakes coated on gas diffusion layer (GDL) were then characterized using scanning electron microscopy, Raman spectroscopy, and X-ray photoelectron spectroscopy (Section S1, Supporting Information). Initially, we explored the potential of choline-based amine electrolytes (dissolved in deionized (DI) water) for the CO_2 reduction reaction on the MoS_2 catalyst within a custom-made two-compartment three-electrode electrochemical cell (Section S2, Supporting Information). **Figure 1**a shows the linear sweep voltammetry (LSV) results for 2 M choline chloride, choline bromide, and choline bitartrate solutions. Among the different tested choline-based electrolytes, 2 M choline chloride exhibits the highest current density with the maximum of –210 mA cm^{-2} at –0.8 V versus RHE compared to –120 and –70 mA cm^{-2} for choline bromide and bitartrate solutions, respectively (Figures S2a and S4, Supporting Information). To increase the ionic conductivity of the solution, we added different molar quantities of KOH while keeping the overall salt concentration of the electrolyte constant (2 M). Our results shown in Figures S2a and S4 of the Supporting Information (Section S2, Supporting Information) indicate that electrolyte with the ratio of 1 M choline chloride and 1 M KOH shows a current density of –315 mA cm^{-2} at –0.8 V versus RHE, which is highest among the tested electrolytes. The obtained current density (–315 mA cm^{-2}) in the CO_2 saturated buffer electrolyte (pH ≈ 7.6) is also more than two times higher than that of previously studied acidic electrolyte (pH ≈ 3) 50:50 vol% $EMIMBF_4$ ionic liquid/DI water (–150 mA cm^{-2}) at the potential of –0.8 V versus RHE.[20] At the low potential of –250 mV, the current density of –17.32 mA cm^{-2} is obtained for 1 M KOH/choline chloride, which is ≈1.5 times higher than that of 50:50 vol% $EMIMBF_4$/DI water electrolyte (–11.21 mA cm^{-2}).[20]

We also studied the catalytic activity of MoS_2 NFs in 2 M $KHCO_3$, choline chloride/$KHCO_3$ (1:1 M) and 2 M KOH and compared the results with choline chloride/KOH (1:1 M) electrolyte. Our LSV results in CO_2 saturated electrolytes indicate about 2.5 times higher current density for 2 M KOH (176.6 mA cm^{-2}) compared with 2 M $KHCO_3$ (68.5 mA cm^{-2}). The higher current density is attributed to the higher ionic conductivity of CO_2 saturated KOH compared with $KHCO_3$ electrolyte. Furthermore, adding choline chloride to KOH and $KHCO_3$ increases the current density by a factor of about 1.85 and 1.6, respectively. We attribute this to higher CO_2 solubility in the choline chloride electrolytes making the CO_2 species more available for the reaction on the catalyst surface.

Product characterizations of the choline chloride/KOH (1:1 M) electrolyte at different applied potentials (–0.2 to –0.8 V vs RHE) confirms CO as the main product with an overall Faradaic efficiency of 90% ± 5% (Section S3, Supporting Information). We also performed electrochemical impedance spectroscopy (EIS) measurement (Figure 1b) at the cell potential of –2 V to investigate the effect of charge transfer on the electrochemical performance of tested electrolytes (Section S4, Supporting Information). Results indicate that the choline chloride/KOH system with the 1:1 molar ratio exhibits almost seven and three times lower charge transfer resistance compared to

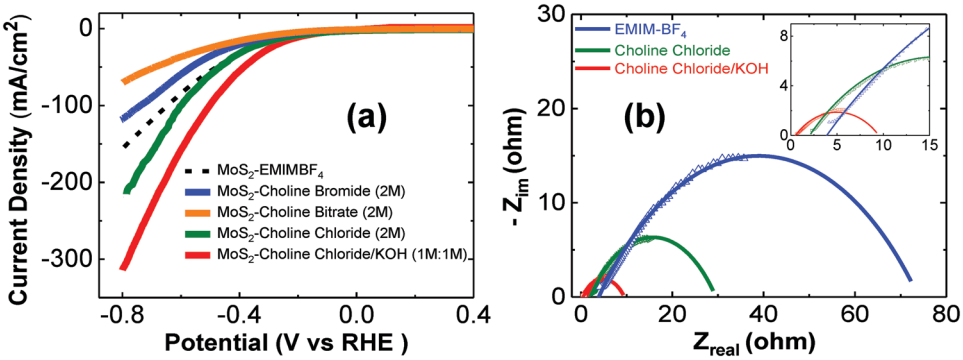

Figure 1. a) Linear sweep voltammetry results of MoS_2 NFs at different choline-based electrolytes (a total concentration of 2 M), 50:50 vol% $EMIMBF_4$/DI water, and choline chloride/KOH (1:1 M) electrolyte. b) Electrochemical impedance spectroscopy of CO_2 reduction by MoS_2 NFs in 50:50 vol% $EMIMBF_4$/DI water, choline chloride (2 M), and choline chloride/KOH (1:1 M) electrolytes at the cell potential of –2.0 V.

© 2019 WILEY-VCH Verlag GmbH & Co. KGaA, Weinheim

50:50 vol% $EMIMBF_4$/DI water and 2 M choline chloride solutions, respectively.[20] The lower charge transfer resistance in choline chloride/KOH electrolyte further confirms the superior current density results in Figure 1a.

Next, we studied the energy efficiency of the CO_2 reduction reaction in a dynamic mode using the same cathode and anode materials. We used a one-compartment cell (Section S5, Supporting Information) instead of a two-compartment cell to avoid a membrane separator between catholyte and anolyte. This is mainly due to unique feature of the electrolyte which uniformly provides high ionic conductivity and high CO_2 solubility. The one-compartment cell configuration reduces the potential loss, leading to an increased cell efficiency during the electrochemical reaction.[23,24] It should be noted that the initial pH of the choline chloride/KOH (1:1 M) solution is about 13.3, which drops to 7.6 after CO_2 saturation due to the formation of bicarbonate ions as discussed, later in the computational part. The electrolyte saturated with CO_2 (pH = 7.6) was cycled in the flow cell at the rate of 0.5 mL min^{-1}. **Figure 2**a shows the current density of the CO_2 reduction reaction obtained from chronoamperometry experiments at different cell potentials (–1.5 to –2.0 V, Section S6, Supporting Information). As shown in Figure 2a the maximum current density of about –185 mA cm^{-2} was obtained at the cell potential of –2.0 V, which is equivalent to 660 mV overpotential considering the thermodynamic potential of –1.34 V for the flow cell. We note that our EIS experiments at different cell potentials show negligible internal resistances in the flow cell (Figure S10 and Section S7 of the Supporting Information).

The product stream analysis of the flow cell shows that the system is largely selective for CO formation at different applied potentials (–1.5 to –2 V), as confirmed by gas chromatography measurement (Section S8, Supporting Information). Our results indicate an F.E. of 93% ± 5%, cell efficiency of about 83% and turnover frequency (TOF) of 4.25 s^{-1} at –1.5 V cell potential (Figure 2b). The maximum TOF of about 10 s^{-1} was recorded at –2.0 V (overpotential of 660 mV), which is fairly comparable to the highest CO_2 reduction TOF reported so far.[20] The calculated cell efficiency, TOF, and F.E. at other cell potentials are presented in Figure 2b.

To examine the stability of the electrolyte, we performed nuclear magnetic resonance (NMR) experiments of the fresh and used electrolytes (KOH: choline chloride = 1:1 M) (Section S9, Supporting Information). The ^1H and ^{13}C NMR spectra confirm the stability of the choline chloride electrolyte in the flow cell experiments without any evidence of electrolyte decomposition. Moreover, we measured the concentration of K^+ via atomic adsorption spectroscopy and pH of the electrolyte in 30 min time intervals during a 15 h continuous process (Section S10, Supporting Information). These results indicate that concentrations of both cations remain fairly constant, suggesting the charge neutrality during the electrochemical process.

To drive the process by solar energy, we coupled the flow cell to a triple junction photovoltaic (TJ-PV) cell with a maximum efficiency of 29.1%. **Figure 3**a depicts the schematic of our solar driven CO_2 conversion process. The *I–V* characteristic curves of the TJ-PV cell with a surface area of 12.8 cm^2 under 1 sun illumination and in the dark mode is depicted in Figure 3b. This surface area is intentionally selected since it could deliver the open circuit voltage and photocurrent of 2 V and –182.5 mA under 1 sun illumination (1 KW m^{-2}), respectively (Figure 3b; Figure S14, Supporting Information). This provides the optimum voltage and total current required by 1 cm^2 area of the catalyst (in the flow cell) at 2 V (Figure 2a). Considering a photocurrent of ≈–182.5 mA at 2.0 V, the total efficiency of the TJ-PV cell is calculated to be 28.5% which is very close to its maximum efficiency (29.1%). The solar-to-fuel efficiency (SFE) was also measured during a 15 h continuous processing of CO_2 while monitoring the current density and voltage simultaneously. As shown in Figure 3c, the process starts with a current density of ≈–182.5 mA cm^{-2} and decays to ≈–175 mA cm^{-2} (red line), implying about 4.9% loss during 15 h of the process. The SFE of the process (Figure 3d) indicates an average value of 18.2% under 1 sun illumination (Section S11, Supporting Information) with a negligible variation during 15 h of the experiment.

To measure SFE with respect to the number of the sun illuminations (Section S12, Supporting Information), the PV cell was calibrated to generate the required photocurrent for the CO_2 reduction reaction at each cell potential by varying the number of sun illuminations (0.5–1 sun). Figure 3e shows the calculated SFE at different sun illuminations. At 0.5 sun illumination, we obtained an SFE of about 23% and a reaction current density of 85.95 mA cm^{-2}. To the best of our knowledge, this is the highest SFE reported for the CO_2 reduction reaction.[14]

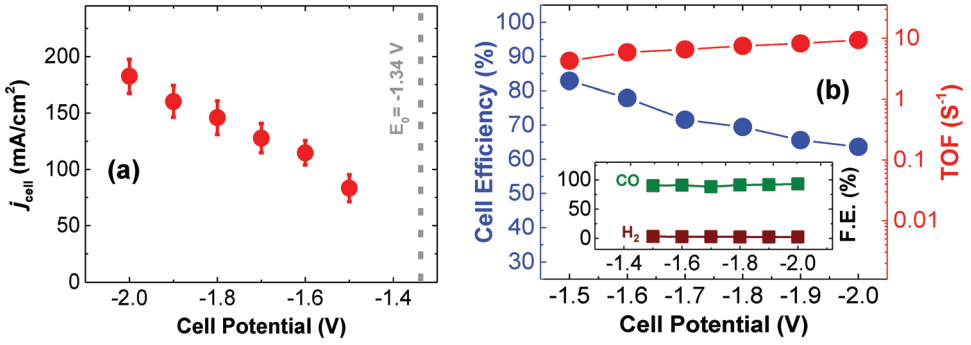

Figure 2. Continuous CO_2 reduction reaction (flow cell) results. a) Current density at different cell potentials. b) Calculated cell efficiency and turnover frequency (TOF) of flow cell at different cell potentials. The flow cell shows the efficiency of ≈83% at –1.5 V and TOF of ≈10 (s^{-1}) at –2.0 V cell potential. (inset) Faradaic efficiency measurement for MoS_2 catalytic system with Choline chloride/KOH (1:1 M) at different cell potentials.

© 2019 WILEY-VCH Verlag GmbH & Co. KGaA, Weinheim

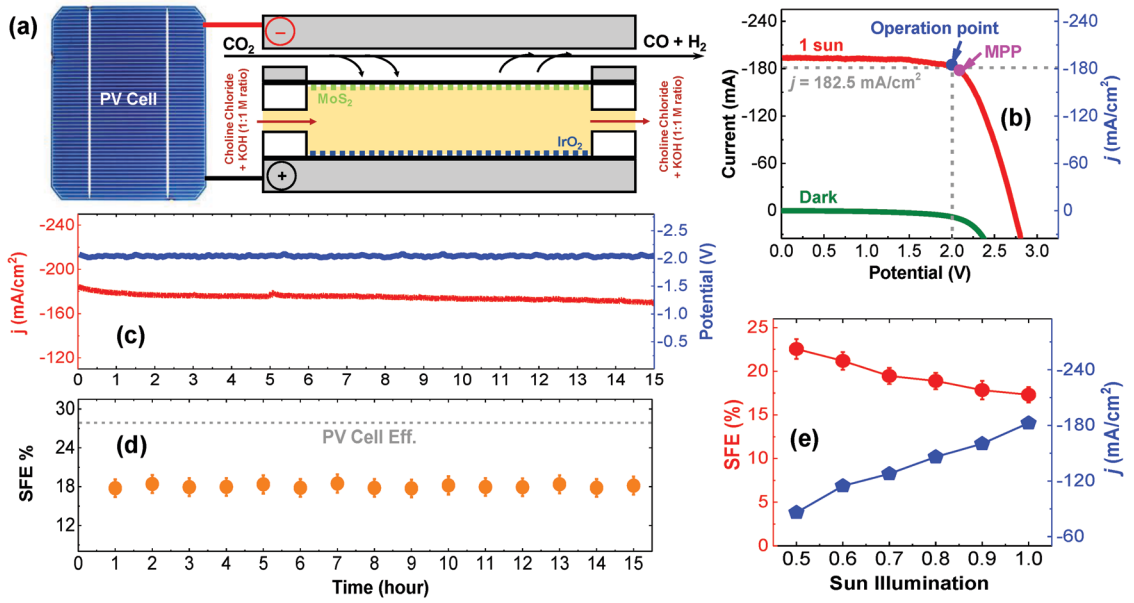

Figure 3. Solar-driven flow cell results. a) A schematic of flow cell using solar energy to drive CO_2 reduction reaction. b) Characteristic curve of the PV-cell with the surface area of 12.8 cm^2 under 1 sun illumination and also in the dark mode. The operational point based on the performance of flow cell (electrolyzer) as well as maximum power point (MPP) is also shown in this figure. c) The current density of reaction and input potential during 15 h process under 1 sun illumination. The current density of about −180 mA cm^{-2} and potential of −2.00 V were recorded during the process. d) Solar to fuel efficiency of flow cell under 1 sun illumination during 15 h process. The process shows an average SFE of 18.2% during the photoelectrochemical reaction that is limited by PV cell efficiency (≈29.1%). e) Solar to fuel efficiency of flow cell with respect to the number of the sun illumination. The results show 23% solar to fuel efficiency at 0.5 sun illumination.

Classical molecular dynamics (MD) simulations, ab initio molecular dynamics (AIMD), and density functional theory (DFT) calculations were performed to gain insights into the mechanisms behind the CO_2 reduction in the choline chloride/KOH and MoS_2 NFs system.

In order to gain a better understanding of the molecular interactions of different species during the CO_2 reduction process, we first carried out classical MD simulations. We observed that in equilibrium, the region of highly concentrated OH^- anions almost coincides with the first density peak of the CO_2 molecules (see **Figure 4**b). Accordingly, we performed DFT-based AIMD simulations, and observed that among different species inside the system, the CO_2 and the OH^- bind together to form a HCO_3^- ion (see the trajectory snapshots in **Figure 5**a). This suggests that the OH^- ions react with the added CO_2 molecules to form bicarbonate anions. Previous reports[25,26] for CO_2 reduction on metal electrodes suggest HCO_3^- formation from CO_2 and OH^- in buffered electrolytes at near neutral pH. This is also supported by the experimental observation that CO_2 saturated choline chloride/KOH electrolyte has a pH of around 7.6.

Next, we carried out DFT calculations to further investigate the reaction mechanism and to study the possible role of bicarbonate ions in facilitating CO_2 exchange toward the MoS_2 edge sites[27] (Section S13.2, Supporting Information). Figure 5b shows that the presence of the HCO_3^- ion and a H_2O molecule facilitate the CO_2 exchange via bond breaking/forming with a low free energy barrier of 0.19 eV. Figure 4b shows that the first density peaks of HCO_3^- ions and CO_2 molecules are almost at the same location, close to the negatively charged MoS_2 cathode surface (≈1.7 Å away from the MoS_2 edge sites), suggesting that HCO_3^- ions and CO_2 molecules can participate in the low barrier CO_2 exchange process to supply sufficient reactants for the electrochemical reactions. Moreover, our results indicate that the cathode surface exhibits a strong propensity for the K^+ adsorption over the choline molecules. This is supported by the penetration of K^+ ions between the MoS_2 NF interlayer spaces (Figure 4a), exhibiting a high-density peak at ≈−2 Å relative to the outermost Mo edge atoms. The adsorption of the bulky choline cations onto the MoS_2 edges is impeded due to their unfavorable electrostatic interactions with the accumulated K^+ ions (Figure S28 and Section S14 of the Supporting Information). Thus, the depletion of choline molecules in the electric double layer region and the smaller size and steric effects of K^+ atoms expose more catalyst active sites for CO_2 reduction.

Our electrochemical experiments for choline chloride/KOH electrolytes were carried out under nearly neutral, i.e., pH ≈ 7.6 condition that is consistent for a long period of time (15 h). This indicates the overall concentrations of both OH^- and H^+ are extremely low during the reaction. This is likely due to the considerable amount of HCO_3^- ion in the electrolyte, acting as a pH buffer. The CO_2 and proton concentrations at the cathode depend on both mass transfer that determines their supply rate and the current density that determines their consumption rate. While the oxygen evolution reaction on the anode generate protons,[28] CO_2 reduction at nearly neutral pH and high current densities is likely limited by the cathode side as was shown to be the case for metal electrodes.[25,26]

Thus we propose that for the MoS_2 cathode reactions at low overpotentials water molecules could instead act as proton

© 2019 WILEY-VCH Verlag GmbH & Co. KGaA, Weinheim

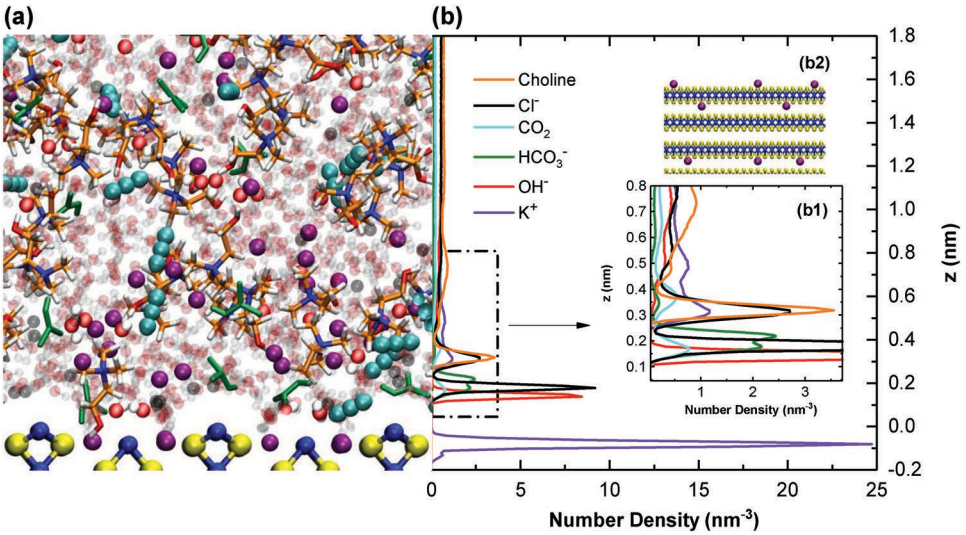

Figure 4. Classical MD simulation results. a) Snapshot of classical MD simulation trajectory of choline chloride/KOH/$KHCO_3$ (1:1:1 M) electrolyte system with MoS_2 nanoflakes. Water molecules are represented by transparent spheres and Mo and S atoms are illustrated by blue and yellow colors, respectively. The color for the rest of the species are given in the legend of (b). b) Center of mass number density profiles of the choline chloride/KOH/$KHCO_3$ (1:1:1 M) electrolyte system with MoS_2 nanoflakes. The lower inset (b1) is the zoomed-in electric double layer (EDL) region close to the MoS_2 interface. The upper inset (b2) is a snapshot of K^+ ions coverage on the MoS_2 surface. The dashed blue line indicates the zero on the *z*-axis, which is set to the outermost Mo edge atoms location.

donors for CO_2 reduction and release OH^- ions. We hypothesize that at low overpotentials in a steady-state mode, these OH^- ions could be consumed again by the CO_2 molecules near the cathode to form HCO_3^- (similar to the process shown in Figure 5a). The generated OH^- ions could also react with HCO_3^- ($HCO_3^- + OH^- = H_2O + CO_3^{2-}$) resulting in a steady state distribution of CO_3^{2-} and HCO_3^- and the generated protons from the anode[28] that satisfies mass transfer requirements. Therefore, we carried out DFT calculations to investigate possible reaction pathways on MoS_2 cathode that could result

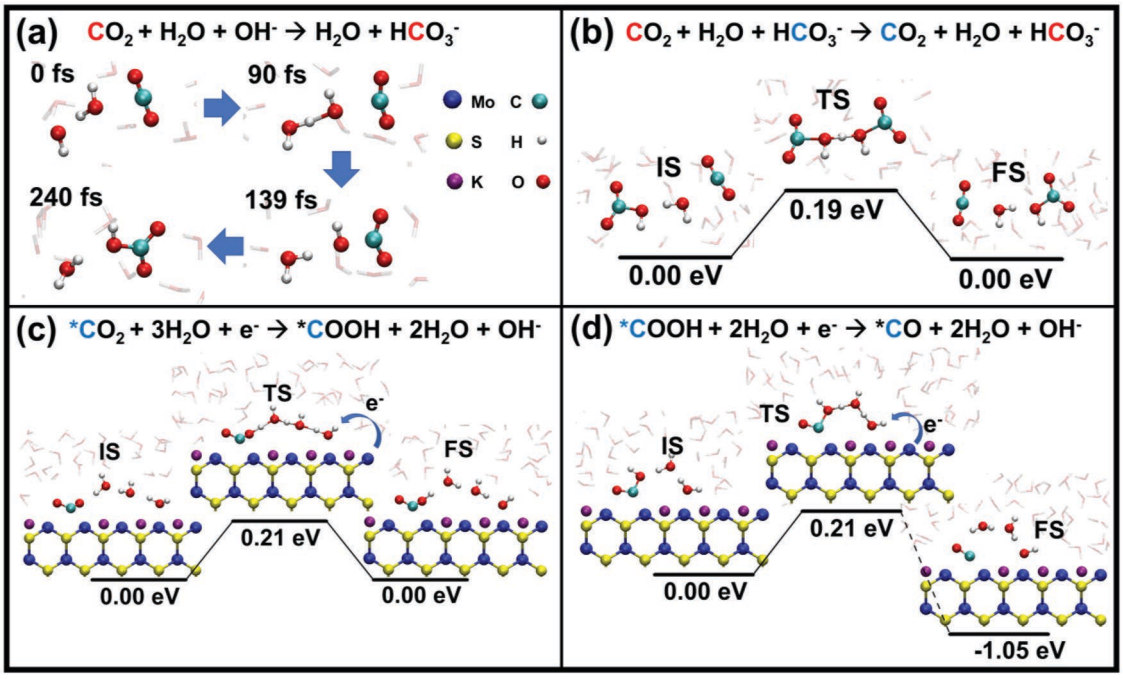

Figure 5. Density functional theory results. a) DFT-based AIMD trajectory snapshots, showing HCO_3^- formation. b–d) DFT CI-NEB calculation results for different steps in CO_2 reduction process. b) CO_2 exchange process, (c) *COOH (* representing adsorbates) formation, and (d) C—OH bond breaking to produce *CO. The initial state (IS), transition state (TS), and the final state (FS) associated with their corresponding free energies (ΔG) are shown. In all the CI-NEB calculations, the solvation corrections are calculated by adding water molecules in the first solvation shell around the species, followed by the structural relaxations (Section S13, Supporting Information).

© 2019 WILEY-VCH Verlag GmbH & Co. KGaA, Weinheim

in low overpotentials with H_2O as the proton donor. As shown in Figure 5c, one H_2O molecule near the Mo edge splits, and the dissociated proton transports through the hydrogen bond chain, reaching the $*CO_2$ to form the *COOH complex with free energy barrier of 0.21 eV. The relatively low free energy barrier indicates a fast process of *COOH formation with H_2O molecules donating protons (Figure 5c). We note that this reaction mechanism, in which the water acts as a proton donating agent under a neutral pH condition (pH ≈ 7.6) is very different from the previously studied $EMIMBF_4$ ionic liquid electrolyte system,[20] where the main source of protons was the H^+ ions in the acidic environment (pH ≈ 3).

Figure 5d shows the subsequent process of C—OH bond breaking aided by proton transport to form *CO. Similarly, one H_2O molecule splits near the Mo edge and the dissociated proton approaches the —OH group of the *COOH by transferring through the hydrogen bond chain. The C—OH bond finally breaks and a new H_2O molecule is formed. This process has a small free energy barrier of 0.21 eV. The newly formed H_2O molecule reorients itself to form hydrogen bonds with the neighboring H_2O and *CO, which further lowers the total energy and makes the whole reaction strongly exergonic, with the formation free energy of −1.05 eV.

For the desorption of produced CO from the cathode surface, our calculations show that when the CO coverage is 1 monolayer (ML), the binding energy per CO on a Mo atom is 0.92 eV (Table S4, Section S13.6, Supporting Information). However, when the CO coverage on the MoS_2 surface is increased to 2 ML after accumulation of CO, the binding energy for the second CO on a Mo atom decreases to 0.35 eV. These results suggest that during the electrochemical reactions, the Mo edges of the MoS_2 NF cathodes would have high CO coverage (>1 ML) to make the CO desorption easier. This is also consistent with our previous study.[20]

3. Conclusion

We have demonstrated a continuous solar-driven electrocatalysis process that effectively converts CO_2 to CO. Our results indicated that nanostructured MoS_2 catalyst inside an inexpensive hybrid electrolyte of choline chloride/KOH exceed the CO_2 reaction rate of previously studied expensive $EMIMBF_4$ ionic liquid. Using a solar-driven single compartment flow cell we obtained a maximum solar to fuel and catalytic conversion efficiencies of 23% and 83%, respectively, tested up to 15 h of continuous process. Our classical MD, AIMD, and DFT simulations revealed that the superior CO_2 reduction performance of the choline chloride/KOH and MoS_2 NFs system could be attributed to: (i) the accumulation of K^+ ions near the MoS_2 surface displacing the bulky choline cations, leading to higher availability of the active sites; (ii) binding of OH^- and CO_2 to form HCO_3^- ions, which could enhance the effective CO_2 concentration close to the cathode through equilibrium exchange as well as participate in mass transfer; and (iii) water molecules near the cathode that act as proton donors to facilitate the reduction process by MoS_2 cathodes.

4. Experimental Section

Electrolyte Preparation: different choline base salts, i.e., choline chloride, choline bromide, and choline bitartrate, and KOH were purchased from Sigma-Aldrich and diluted with deionized water (18.2 MΩ) until desired concentrations.

Catalyst Preparation: MoS_2 NFs were synthesized using a modified liquid exfoliation method. In brief, 300 mg MoS_2 powder synthesized by chemical vapor transport method was dispersed in 60 mL isopropanol solution and sonicated for 20 h using sonication probe (Vibra Cell Sonics 130W). The solution was then centrifuged for about 60 min to separate nanoflakes with average size of about 100 nm from its bulk media. IrO_2 nanopowder (50 nm) was purchased from Alfa Aesar. The powder was dispersed in DI water and IPA solution with w/vol ratio of 10(w):0.6(v):0.6(v) and coated on GDL for electrochemical experiments.

Electrochemical Experiments: Three-electrode electrochemical experiments were carried out using a custom designed two compartment three-electrode electrochemical cell. The synthesized MoS_2 NFs coated on porous GDL substrate via layer by layer deposition process was used as a working electrode. Platinum mesh (gauze 52 mesh, Alfa Aesar) and Ag/AgCl (BASi) were used as counter and reference electrodes, respectively. Different choline-based electrolytes at desired concentrations, e.g., 0.5, 1, and 2 M were used as electrolytes. The voltage was swept between +0.4 and −0.8 V versus RHE with 50 mV s^{-1} scan rates. LSV curve was then recorded using a Voltalab PGZ100 potentiostat (purchased via Radiometer Analytical SAS) calibrated with a RCB200 resistor capacitor box. The potentiostat was connected to a PC using Volta Master (version 4) software. All flow cell experiments were also performed in a custom-designed one compartment electrochemical cell (Figure S8, Supporting Information) consisting of MoS_2 NFs deposited on GDL as a cathode, IrO_2 nanopowder coated on GDL as the anode and CO_2 saturated 1:1 M choline chloride/KOH as the electrolyte (Section S5, Supporting Information). The reactor was also connected to a TJ-PV solar cell in order to power with solar energy. The PV cell was provided by a local company, Micro-Link Device, Inc. at Chicago. More detailed information can be found in the following link: http://mldevices.com/index.php/product-services/photovoltaics

Computational Details: Density functional theory calculations and ab initio molecular dynamics simulations. The detailed reaction mechanisms of CO_2 reduction at MoS_2 cathode surface were studied with DFT method using VASP package.[29,30] The Perdew–Burke–Ernzerhof exchange-correlation functional was employed.[31] The plane wave basis sets were used for periodic system calculations, with a kinetic energy cutoff of 400 eV. All structural relaxation processes were identified as converged until the maximum residual forces were smaller than 0.05 eV $Å^{-1}$. Spin-polarized calculations were used for all systems involving MoS_2 NFs. For the k-point grids, unless otherwise mentioned, gamma-point was used for all the molecular species and gamma-centered 4 × 1 × 1 k-grids was used for periodic systems involving crystals. AIMD simulations were carried out to study the interactions between different species in the choline chloride/KOH system. All AIMD simulations were performed using the time step of 1 fs. The NVT ensemble was applied to the system at the temperature of 298 K. Climbing image nudged elastic band (CI-NEB) method[32,33] was used to explore the CO_2 equilibrium exchange process and the MoS_2 surface catalytic properties. The intermediate images were first generated by performing linear interpolation between the geometries of the initial state and the final state. The transition state search was conducted by the Quick-Min force-based optimizer to converge to the saddle point.[34] More details on DFT and AIMD simulations can be found in the Supporting Information.

Classical Molecular Dynamics Simulation: These simulations were carried out using the GROMACS[35] software with time step of 1 fs. The bulk electrolyte systems were initially equilibrated in the NVT ensemble by a simulated annealing procedure. The final configuration was equilibrated for 2 ns followed by a production run of 10 ns in the NPT

© 2019 WILEY-VCH Verlag GmbH & Co. KGaA, Weinheim

ensemble at the pressure of 1atm and temperature of 298.15 K. The temperature and pressure were kept constant using the Nosé–Hoover thermostat,[36,37] and Parrinello–Rahman barostat[38] with the time constants of 0.2 and 1 ps, respectively. Periodic boundary conditions were applied in all directions. The details about the force field and interactions between different species are given in the Supporting Information. Trajectories of the atoms were collected every 1 ps to obtain the results. The bulk density and self-diffusion coefficient of different species were calculated using the final 6 ns trajectories of the NPT production simulation. For the confined systems, the electrolyte is sandwiched between two blocks of vertically aligned MoS_2 sheets separated by a surface-to-surface distance of 17 nm in the *z* direction. Each block consists of 12 vertically aligned MoS_2 sheets each extended in the *x*–*z* plane with Mo terminated edge atoms pointing toward the electrolyte. The lateral dimensions of the sheets were 7.111×7.080 nm^2. A periodic boundary condition was applied in all the directions with an extra vacuum of 33 nm in the *z* direction to avoid slab–slab interactions between periodic images. During the simulation, the MoS_2 sheets were frozen, i.e., their positions were not updated. The electrolytes close to the negatively charged MoS_2 wall with charge density of $\sigma_w = -0.053$ e nm^{-3} were simulated. For more detail regarding the simulation setup, force fields, and results; please refer to the Supporting Information.

Supporting Information

Supporting Information is available from the Wiley Online Library or from the author.

Acknowledgements

M.A. and M.H.M. contributed equally to this work. A.S.-K. R.B., P.A., and L.M.'s work was supported by the National Science Foundation (NSF, Grant #NSF-CBET-1512647 and NSF-DMREF Award #1729420). T.V.S., M.H.M, A.M., and N.R.A. were supported by the NSF under Grant Nos. 1420882, 1506619, 1545907, and 1708852. The authors acknowledge the use of the parallel computing resource Blue Waters provided by the University of Illinois and the National Center for Supercomputing Applications. C.L.'s work at Argonne National Laboratory (ANL) was supported by the U.S. Department of Energy (DOE), Office of Basic Energy Sciences, Division of Chemical Sciences, Geosciences, and Biosciences, under Contract No. DE-AC02-06CH11357, with UChicago Argonne, LLC, the operator of ANL. L.A.C. and P.Z.'s efforts were supported by DOE, Office of Science, BES-Materials Science and Engineering, under Contract No. DE-AC-02-06CH11357, with UChicago Argonne, LLC, the operator of ANL. M.A. and M.E.'s work were supported by Illinois Institute of Technology start-up funding, Wanger Institute for Sustainable Energy Research (WISER) seed fund (262029 221E 2300) and the Soft and Hybrid Nanotechnology Experimental (SHyNE) Resource seed funding at Northwestern University. The authors also acknowledge Dr. Rao Tatavarti from Micro-Link Device, Inc. at Chicago for providing the triple junction PV cell and Lisha Wu at the University of Illinois at Chicago for potassium (K^+) analysis. A.S.-K. and M.A. conceived the idea. M.A. performed the flow cell and solar driven electrochemical experiments. M.A., L.M., M.E., R.B., and P.A. performed three electrode experiments and characterizations. A.S.K. supervised the electrochemical and characterization experiments. M.H.M. and A.M. performed classical MD simulations, T.V.S. performed DFT calculations, all under the supervision of N.R.A., C.L., P.Z., and L.A.C. contributed to the DFT calculation. A.K. performed flame atomic absorption spectroscopy experiments.

Conflict of Interest

The authors declare no conflict of interest.

Keywords

flow cells, photochemical, photoelectrochemical, solar to fuel conversion

Received: November 15, 2018
Revised: December 17, 2018
Published online: January 21, 2019

[1] Z. W. She, J. Kibsgaard, C. F. Dickens, I. Chorkendorff, J. K. Nørskov, T. F. Jaramillo, *Science* **2017**, *355*, eaad4998.
[2] J. H. Montoya, L. C. Seitz, P. Chakthranont, A. Vojvodic, T. F. Jaramillo, J. K. Nørskov, *Nat. Mater.* **2017**, *16*, 70.
[3] S. Chu, Y. Cui, N. Liu, *Nat. Mater.* **2017**, *16*, 16.
[4] H. B. Gray, *Nat. Chem.* **2009**, *1*, 7.
[5] S. Dahl, I. Chorkendorff, *Nat. Mater.* **2012**, *11*, 100.
[6] A. Listorti, J. Durrant, J. Barber, *Nat. Mater.* **2009**, *8*, 929.
[7] T. R. Cook, D. K. Dogutan, S. Y. Reece, Y. Surendranath, T. S. Teets, D. G. Nocera, *Chem. Rev.* **2010**, *110*, 6474.
[8] K. Sun, S. Shen, Y. Liang, P. E. Burrows, S. S. Mao, D. Wang, *Chem. Rev.* **2014**, *114*, 8662.
[9] K. S. Joya, Y. F. Joya, K. Ocakoglu, R. Van De Krol, *Angew. Chem., Int. Ed.* **2013**, *52*, 10426.
[10] Z. Li, J. Feng, S. Yan, Z. Zou, *Nano Today* **2015**, *10*, 468.
[11] S. N. Habisreutinger, L. Schmidt-Mende, J. K. Stolarczyk, *Angew. Chem., Int. Ed.* **2013**, *52*, 7372.
[12] G. Centi, S. Perathoner, *ChemSusChem* **2010**, *3*, 195.
[13] G. Centi, S. Perathoner, *Greenhouse Gases: Sci. Technol.* **2011**, *1*, 21.
[14] M. Schreier, F. Héroguel, L. Steier, S. Ahmad, J. S. Luterbacher, M. T. Mayer, J. Luo, M. Grätzel, *Nat. Energy* **2017**, *2*, 17087.
[15] F. Sastre, A. V Puga, L. Liu, A. Corma, H. García, *J. Am. Chem. Soc.* **2014**, *136*, 6798.
[16] S. Y. Reece, J. A. Hamel, K. Sung, T. D. Jarvi, A. J. Esswein, J. J. H. Pijpers, D. G. Nocera, *Science* **2011**, *334*, 645.
[17] A. Rabis, P. Rodriguez, T. J. Schmidt, *ACS Catal.* **2012**, *2*, 864.
[18] P. D. Tran, L. H. Wong, J. Barber, J. S. C. Loo, *Energy Environ. Sci.* **2012**, *5*, 5902.
[19] B. Winther-Jensen, D. R. MacFarlane, *Energy Environ. Sci.* **2011**, *4*, 2790.
[20] M. Asadi, K. Kim, C. Liu, A. V. Addepalli, P. Abbasi, P. Yasaei, P. Phillips, A. Behranginia, J. M. Cerrato, R. Haasch, P. Zapol, B. Kumar, R. F. Klie, J. Abiade, L. A. Curtiss, A. Salehi-Khojin, *Science* **2016**, *353*, 467.
[21] M. Asadi, B. Sayahpour, P. Abbasi, A. T. Ngo, K. Karis, J. R. Jokisaari, C. Liu, B. Narayanan, M. Gerard, P. Yasaei, X. Hu, A. Mukherjee, K. C. Lau, R. S. Assary, F. Khalili-Araghi, R. F. Klie, L. A. Curtiss, A. Salehi-Khojin, *Nature* **2018**, *555*, 502.
[22] L. Majidi, P. Yasaei, R. E. Warburton, S. Fuladi, J. Cavin, X. Hu, B. Sayahpour, I. L. Bolotin, P. Zapol, J. Greeley, R. F. Klie, R. Mishra, F. Khalili-araghi, L. A. Curtiss, A. Salehi-khojin, *Adv. Mater.* **2018**, *1804453*, 1.
[23] S. Verma, X. Lu, S. Ma, R. I. Masel, P. J. A. Kenis, *Phys. Chem. Chem. Phys.* **2016**, *18*, 7075.
[24] S. Ma, R. Luo, S. Moniri, Y. Lan, P. J. A. Kenis, *J. Electrochem. Soc.* **2014**, *161*, F1124.
[25] N. Gupta, M. Gattrell, B. MacDougall, *J. Appl. Electrochem.* **2006**, *36*, 161.
[26] M. R. Singh, E. L. Clark, A. T. Bell, *Phys. Chem. Chem. Phys.* **2015**, *17*, 18924.
[27] M. Dunwell, Q. Lu, J. M. Heyes, J. Rosen, J. G. Chen, Y. Yan, F. Jiao, B. Xu, *J. Am. Chem. Soc.* **2017**, *139*, 3774.

 © 2019 WILEY-VCH Verlag GmbH & Co. KGaA, Weinheim

[28] Y. Hori, in *Modern Aspects of Electrochemistry NO 42* (Eds: C. G. Vayenas, R. E. White, M. E. Gamboa-Aldeco), Springer, New York **2008**, pp. 89–189.
[29] G. Kresse, J. Furthmüller, *Comput. Mater. Sci.* **1996**, *6*, 15.
[30] G. Kresse, J. Furthmüller, *Phys. Rev. B* **1996**, *54*, 11169.
[31] J. P. Perdew, K. Burke, M. Ernzerhof, *Phys. Rev. Lett.* **1996**, *77*, 3865.
[32] G. Henkelman, H. Jónsson, *J. Chem. Phys.* **2000**, *113*, 9978.
[33] G. Henkelman, B. P. Uberuaga, H. Jónsson, *J. Chem. Phys.* **2000**, *113*, 9901.
[34] D. Sheppard, R. Terrell, G. Henkelman, *J. Chem. Phys.* **2008**, *128*, 134106.
[35] M. J. Abraham, T. Murtola, R. Schulz, S. Páll, J. C. Smith, B. Hess, E. Lindah, *SoftwareX* **2015**, *1–2*, 19.
[36] S. Nosé, *J. Chem. Phys.* **1984**, *81*, 511.
[37] W. G. Hoover, *Phys. Rev. A* **1985**, *31*, 1695.
[38] M. Parrinello, A. Rahman, *J. Appl. Phys.* **1981**, *52*, 7182.

© 2019 WILEY-VCH Verlag GmbH & Co. KGaA, Weinheim